Shift Current in Molecular Crystals Possessing Charge-Transfer Characteristics

Ali Ebrahimian,[1,*] Mehrdad Dadsetani,[2] and Reza Asgari[1,3,†]

[1]*School of Physics, Institute for Research in Fundamental Sciences (IPM), Tehran 19395-5531, Iran*
[2]*Department of Physics, Lorestan University, Khoramabad 68151-44316, Iran*
[3]*School of Physics, University of New South Wales, Kensington, NSW 2052, Australia*

Further research on organic molecule crystals with spontaneous polarization as a possible candidate for the bulk photovoltaic effect is urgently needed to meet the requirements for optoelectric devices. We demonstrate the shift current in a type of molecular crystal that acts at high temperatures and contains organic molecules with electron donor-acceptor groups, such as paranitroaniline derivatives. We find an extremely strong multicomponent shift-current response along the parallel and perpendicular to polar molecules of the crystals using density-functional simulations, which is more than 10 times larger than the previously reported value for shift current over a broad spectral range from visible to ultraviolet spectrum. Even more intriguing, the remarkable dependency of the conduction- and valence-band dispersions on the lattice constant along polarization allows the shift current in these organic molecule structures to be tuned under stress and doping. Our findings not only suggest a class of organic compounds for realizing the highly controllable shift-current response, but also open up a channel for the search for solar materials.

I. INTRODUCTION

The nonlinear shift current generated by polarized light in single-phase materials with broken inversion symmetry is one of the most efficient methods for converting light directly into electricity [1–6] without the limitations of the Shockley Quisser [7] and precise interface technology in conventional solar cells with p-n junction [8,9]. The shift current, which is a dc, arises from the real-space displacements of the conduction and valence Bloch electrons created during the optical transition and can be expressed in terms of a topological quantity formalism, the Berry connection [10], that was introduced by von Baltz and Kraut [11] to explain the bulk photovoltaic effect (BPVE) in BaTiO$_3$. In fact, the average spacing and direction of the Bloch electron shift (shift vector) [12,13] is determined by the difference in the Berry connection of the Bloch wave functions of the conduction and valence bands, which have long been known to be nonzero in noncentrosymmetric crystals. Subsequently, BPVE has been intensively studied in ferroelectric oxides due to the lack of inversion symmetry in these materials. Furthermore, the relation between displacement vector and electronic polarization (P_{el}) between conduction and valence bands [14] has motivated recent studies to consider the shift current in materials with large P_{el} [15,16].

First-principles simulations have been used to calculate shift current in various materials [8,9,17–19]. From photocurrent response measurements and first-principles calculations, a shift current in the low-temperature phase (<81 K) of the organic molecular crystal tetrathiafulvalen-p-chloranil (TTF-CA) [20] with a large ferroelectric polarization has been recently reported [15,16]. As an organic charge-transfer (CT) complex, TTF-CA consists of alternating electron donor (D = TTF) and electron acceptor (A = CA) molecules along the a axis [15,21–23]; the transforms upon cooling at $T = 81$ K from a neutral to an ionic phase with large electric polarization along the stacking direction. The CT between neighboring DA molecules (intermolecular CT) in the low-temperature phase (<81 K) is the main contributor to this large polarization along the stacking direction. Although this was a major achievement in the design of efficient solar cells, the main disadvantage for the commercial exploitation of this photovoltaic organic material is its low operating temperature. Fortunately, however, there is an alternative way to achieve large electric polarization in organic materials, in which the CT can occur within molecules (intramolecular CT) with electron donor-acceptor groups. These conjugated systems with intramolecular CT have been studied [24] for their high hyperpolarizability and made in experiment by growing them from methanol at room temperature. Here we show the use of organic molecules with electron donor-acceptor groups, such as the derivatives of paranitroaniline (pNA) (2-methyl-4-nitroaniline and

---

2-amino-4-nitroaniline); alternative approach is to achieve higher operating temperatures for photovoltaic organic crystals. 2-amino-4-nitroaniline (ANA) [24] and 2-methyl-4-nitroaniline (MNA) [25,26] crystallize in noncentrosymmetric crystal structures functioning at low and room temperatures, and their molecular units contain donor ($-NH_2$) and acceptor ($-NO_2$) groups located at opposite ends of the molecule. A material that hosts a large electron polarization is a promising candidate that shows a large shift current. Previous experimental and theoretical studies have taken into account the nonlinear optical properties of these organic crystals, which result from the CT properties of their molecules [24,27,28].

In this paper, we study the electronic structure and shift current of ANA and MNA molecular crystals by utilizing first-principle calculations in the presence and absence of external uniaxial strain. We focus only on the shift current and therefore the scattering processes and the ballistic current are ignored in this work. Our first-principles calculations show that they are polar molecules and have a large density of states. Near the band edge, these organic crystals can generate a large shift current that is more than 10 times larger than the previously reported shift-current

value. We find that by applying the tensile and compressive stress along the direction parallel to the polar axis of the molecules, we can tune their shift current in the visible light energy range. In other words, by using uniaxial stretching as a powerful tool to modulate band dispersion and splitting, ANA (MNA) molecular crystal is a highly efficient platform to achieve high operating temperatures (room temperature) for shift current.

The structure of the paper is as follows. In Sec. II, we briefly introduce the simulation methods. Section III is devoted to the numerical results of the study, focusing on the electronic and shift current of the ANA and MNA molecular crystal structure. Finally, we summarize our results in Sec. IV.

II. THEORETICAL AND COMPUTATIONAL METHODS

Recent calculations using density-functional simulations are available [29,30]. The electronic structures are calculated using density-functional simulations, which are implemented in WIEN2K [31] and QUANTUM ESPRESSO [32] code packages to meet high-accuracy requirements.
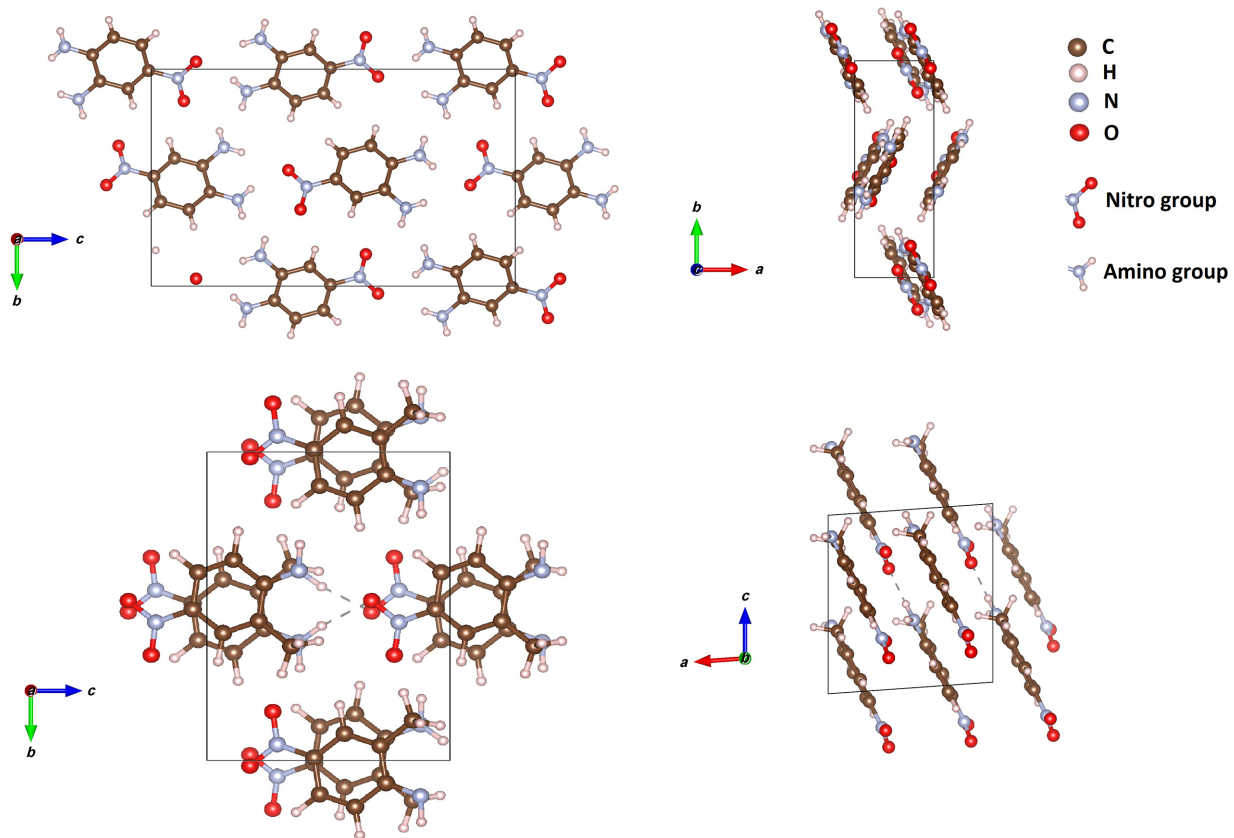

FIG. 1. The crystal structure of 2-amino-4-nitroaniline (ANA) (top panel) and 2-methyl-4-nitroaniline (MNA) (bottom panel) at high-temperature phases. ANA crystallizes in noncentrosymmetric orthorhombic $P2_12_12_1$ structure containing four molecules in the unit cell and MNA crystallizes in the monoclinic system with space group Ia.

PBE-type [33] generalized-gradient-approximation functional is chosen for the electron exchange-correlation energy calculations. A $12 \times 8 \times 5$ ($7 \times 4 \times 6$) Monkhorst pack k-point mesh is used in the computations of electronic structures of the ANA (MNA). Crystal lattices and the internal coordinates of all structures are relaxed in a way that every component of forces is less than 10^{-4} eV/Å. For considering the effects of strain, the uniaxial strain is defined as $(a - a_0)/a_0$, where a_0 and a are lattice parameters without and with strain, respectively, and a_0 is scaled up to $\pm 5\%$. The shift-current tensor is calculated from the formulation of Sipe and Shkrebtii [9,14,34–37], which is implemented in Wannier90 [38,39]. The shift response tensor along direction a induced by bc polarized light, shown in Fig. 1, can be expressed as

$$
\sigma_{\mathbf{abc}}^{\text{shift}}(0; \omega, -\omega)
$$
$$
= \frac{i\pi |e|^3}{4\hbar^2} \int_{BZ} \frac{d\mathbf{k}}{2\pi^3} \sum_{n,m} f_{nm\mathbf{k}}(r_{nm\mathbf{k}}^b r_{nm\mathbf{k}}^{c;a} + r_{nm\mathbf{k}}^c r_{nm\mathbf{k}}^{b;a})
$$
$$
\times [\delta(\omega_{mn\mathbf{k}} - \omega) + \delta(\omega_{nm\mathbf{k}} - \omega)] \qquad (1)
$$

where, $f_{nm\mathbf{k}} = f_{n\mathbf{k}} - f_{m\mathbf{k}}$ is the difference between occupation factors, $\omega_{mn\mathbf{k}} = \omega_{m\mathbf{k}} - \omega_{n\mathbf{k}}$ is the band energy difference, $r_{nm\mathbf{k}}^b$ is the bth Cartesian component of the dipole matrix elements, $r_{nm\mathbf{k}}^{b;a}$ represents generalized derivatives, which is defined as $r_{nm\mathbf{k}}^{b;a} = \delta_{ka}r_{nm\mathbf{k}}^b - i(A_{nn\mathbf{k}}^a - A_{mm\mathbf{k}}^a)r_{nm\mathbf{k}}^b$, the integral is over the first Brillouin zone. The term A_{mn}^b is the Berry connection matrix given as $A_{mn\mathbf{k}}^b = i < u_{m\mathbf{k}}|\partial_{kb}|u_{n\mathbf{k}} >$, where $|u_{n\mathbf{k}} >$ denotes the cell periodic part of a Bloch eigenstate. To obtain well-converged shift-current spectra, we use dense k-point interpolation meshes of $100 \times 100 \times 100$. The space group $P2_12_12_1$ (Ia) to which the ANA (MNA) belong allows for three (ten) independent nonvanishing components of $\sigma_{abc}(0; \omega, -\omega)$ tensors [39,40]: Xyz, Yxz, and Zxy ($Xxx, Xxz, Xyy, Xzz, Yxy, Yyz, Zxx, Zxz, Zyy,$ and Zzz). Previous studies [41] suggest that the potential excitonic effects on the shift current in thin films can be insignificant. Even though our calculation technique does not incorporate electron-hole interactions, we think that the impact of the exciton in our results should be negligible due to the large band gap and large effective masses.

III. NUMERICAL RESULTS AND DISCUSSIONS

ANA crystallizes in a noncentrosymmetric orthorhombic $P2_12_12_1$ structure [25] containing four molecules in the unit cell, while MNA crystallizes in the monoclinic system with the space group Ia [26] (Fig. 1). Lattice constants and internal coordinates of ANA in high-temperature phase at 293 K are fully optimized and we obtain $a = 3.70, b = 10.249,$ and $c = 17.19$ Å for lattice constants. Using a similar procedure, for MNA we have $a = 7.42, b = 11.79, c = 8.19$ Å, $\alpha = \gamma = 90°,$ and $\beta = 94.04°$ in high-temperature phase. These results are in complete agreement with those data reported in experiment [24,25]. Note that although the DFT calculations are performed at zero temperature, the sample structure details are used in the high-temperature phase. The temperature effects on the electronic structure can only be considered in our calculations as a perturbation (electron-phonon interactions) [42,43].
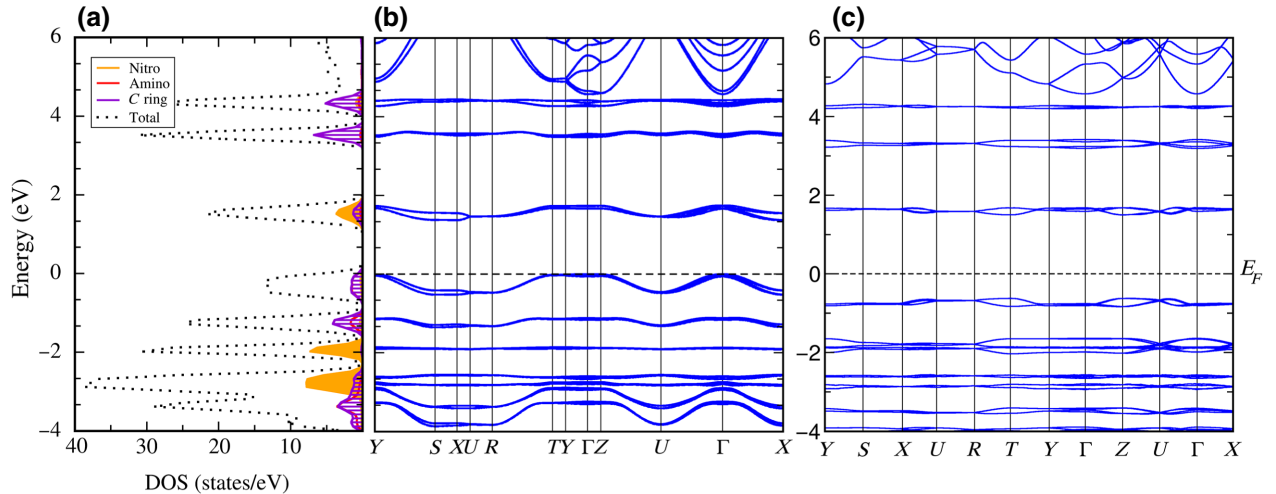

FIG. 2. (a) Calculated total density of states of the ANA and partial density of states for the functional groups of the ANA molecule. The calculated bulk electronic band structure of the ANA (b) and MNA (c). All bands have low dispersions along the high symmetry line of the BZ due to the weak intermolecular interactions. Because of the small intermolecular distance and higher intermolecular interactions the band dispersion is more pronounced in the ANA. The indirect band gaps of 1.36 and 1.91 eV are obtained for ANA and MNA, respectively. The density of states consists mainly of the p states of benzene ring and nitro group.

As shown in Fig. 1, in ANA donor ($-NH_2$) and acceptor ($-NO_2$) groups of the molecules are nearly aligned along the z direction leading to polar molecule with finite polarization ($p_z = 3.4\ \mu C/cm^2$) in unit cell pointing in this direction. Since the polarization of the molecules in the unit cell changes alternately, the total polarization of the unit cell is zero. In MNA, molecules are not fully aligned in the z direction and the polarization of the molecule has nonzero components in the unit cell along the x and y directions ($p_x = 16\ \mu C/cm^2$, $p_y = 0.55\ \mu C/cm^2$, $p_z = 13.4\ \mu C/cm^2$).

In Fig. 2 we plot the electronic band structure and the partial densities of the electronic states of ANA and MNA. As shown, all bands show small dispersions along the high symmetry line of the Brillouin zone (BZ) due to weak intermolecular interactions. Because of the small intermolecular distance and higher intermolecular interactions, the band dispersion is more pronounced in ANA. The PBE calculations give indirect band gaps of 1.36 and 1.91 eV for ANA and MNA, respectively. The partial and total densities of states of the conduction and valence bands of ANA are shown in Fig. 2. The overall DOS consists mainly of the p states of the benzene ring and the nitro group. This figure shows that the lowest conduction bands and highest valence bands consist primarily of the acceptor nitro group ($-NO_2$) and the benzene ring, respectively. As a result, band-edge excitation from the valence band to the conduction band causes the charge density to shift from the benzene ring to the nitro group ($-NO_2$) of molecules.

The calculated band structures at different stress levels and types, illustrated in Fig. 3, show that by applying stress we can tune the band dispersion and splitting of these molecular crystals to improve their photovoltaic efficiency. We systematically apply the uniaxial stretching along the direction parallel to the polar axis of the ANA molecule (z direction) and consider the electronic band structure and the evolution of the optical responses under stretching. Our calculations show that the conduction bands move slightly
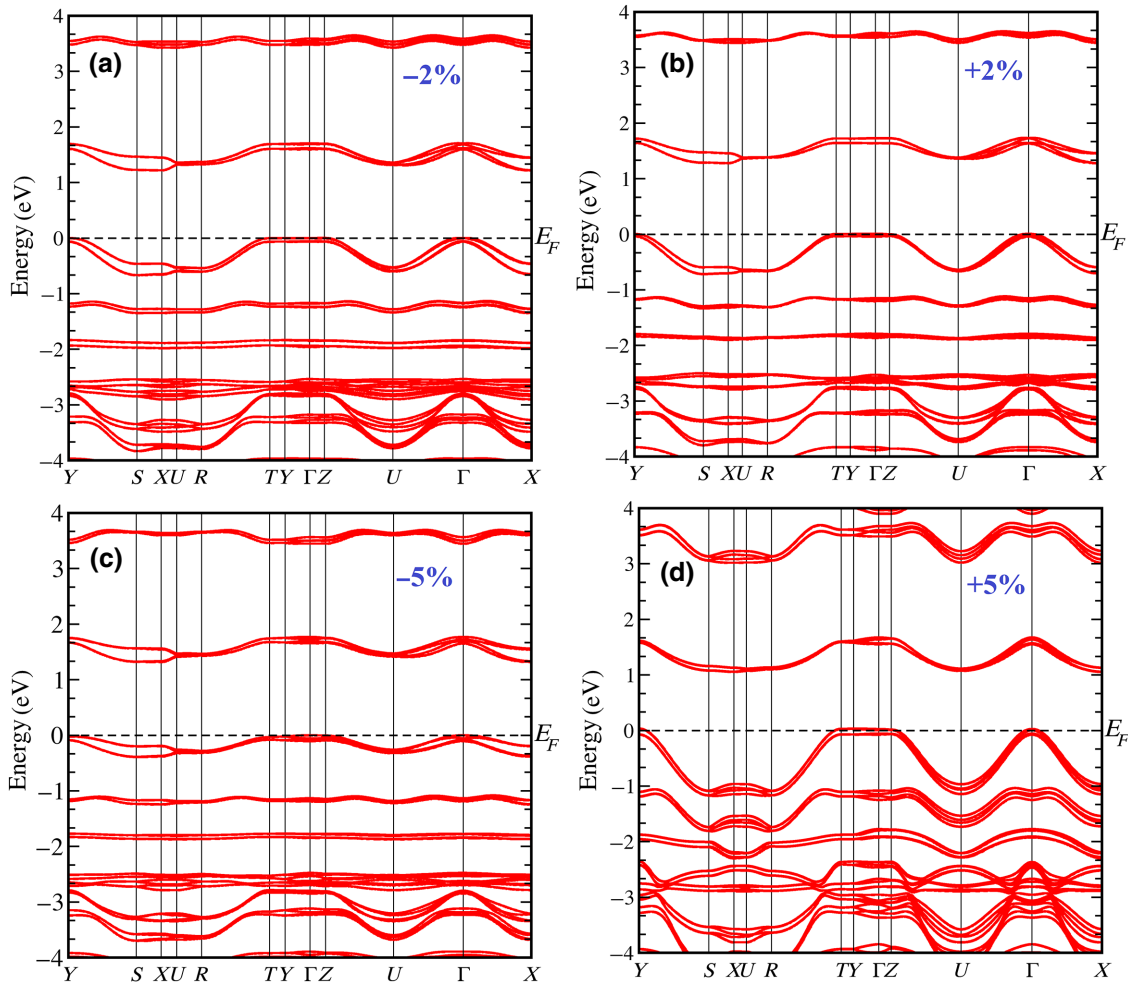

FIG. 3. The calculated band structure of ANA under compressive [(a),(c)] and tensile [(b),(d)] strain. The value of the Fermi energy for +5% strained ANA is shifted down to 0.03 eV below the valence-band minimum to induce 0.1 holes/u.c in the structure. The conduction bands move slightly down (up) under stress, while the shift of the highest valence band is negligible.

down (up) under stress, while the shift of the highest valence band is negligible. Interestingly, the band dispersion and splitting are altered under strain, leading to an increase in the interband transition rate and hence the value and photon energy rate of the shift current.

As already mentioned, the symmetry in ANA allows three independent nonzero components Xyz, Yxz, and Zxy for shift-current-response tensors, where the first letter (capital letter) shows the direction of the shift current and the others the light polarization. As shown in Fig. 4(a), in ANA the shift current is at the same level along all directions in the visible spectrum, which is very desirable for efficient conversion of solar energy. Although the direction of polarization is along the z axis, ANA has a shift-current response along the x and y axes. It is worth noting that the same behavior has been reported in material systems such as single-layer α-In_2Se_3 and $InBiSe_3$ [44].

Except at the onset of photoconductivity, the shift current along z is positive below 4 eV while other components alternate between positive and negative values. The shift current increases above the band gap and reaches 7 $\mu A/V^2$ between 2.5 and 3 eV, resulting from the shift of the space-charge center between the valence bands of the benzene ring and the conduction bands of the nitro group. Above 4 eV all components rapidly oscillate to 6 eV and gradually become positive at higher energies. Note that the peaks are extremely sharp because of the modest band-structure dispersion and the small volume of the unit cell. However, by expanding the grid size to $120 \times 120 \times 120$, we are able to verify the convergence of the computation results.

The calculated shift current of MNA is shown in Fig. 4(b). This figure shows that ten independent components ($Xxx, Xxz, Xyy, Xzz, Yxy, Yyz, Zxx, Zxz, Zyy$, and Zzz) are in principle allowed by symmetry, which contains an extremely large peak compared to those previously

reported in the literature around 50 and 80 $\mu A/V2$ in ferroelectric $PbTiO_3$ (BC_2N-A2) at 6 eV (1.3 eV) [9,45] and chiral crystal RhBiS at 1.3 eV [46]. Put differently, our calculations show the large values for the shift current in MNA with strong peaks of 0.4 and 0.5 mA/V^2 at around 2.3 and 4.5 eV, more than ten times greater than typical reported values for shift current. Each peak in Fig. 4(b) corresponds to an optical transition between one of the conduction and valence bands in the band structure of MNA as illustrated in Fig. 4(c). We extract those transitions based on Eq. (1) since it determines a sum over band-to-band transitions. The detected transitions below 5 eV are indicated in band structures in Fig. 4(c) by vertical arrows. The first (A) transition involves mostly the transitions from the VBM to the CBM band, while the second (B) transition is from the VBM-1 to the CBM bands at the path between $Y(X)$ and Γ points. The D (E) transition is from the VBM (VBM-3) to the CBM+1 (CBM) bands along ΓY and UR.

As shown in Fig. 4(b), MNA has transverse shift-current-response components (Xyy, Xzz, Zxx, and Zyy), where the shift current response is perpendicular to the light polarization. The transverse shift current has a large peak for the shift-current response along the $Z(X)$ axis due to yy polarized light, i.e., Zyy (Xyy). The Zyy component is a dominant initial response with high value. The longitudinal shift-current responses (Zzz) along the Z axis due to zz-polarized light peaks above the band edge while the Xxx component is negligible. In comparison, the transverse shift current for MNA is larger than the longitudinal one in all energy ranges. Among other components, Yyz shows a strong increase to 0.2 $\mu A/V^2$ in the phonon energy window (2–3 eV). Therefore, our result shows that MNA is a molecular crystal with a large shift current and multicomponent photoconductivity. In spite of the structural
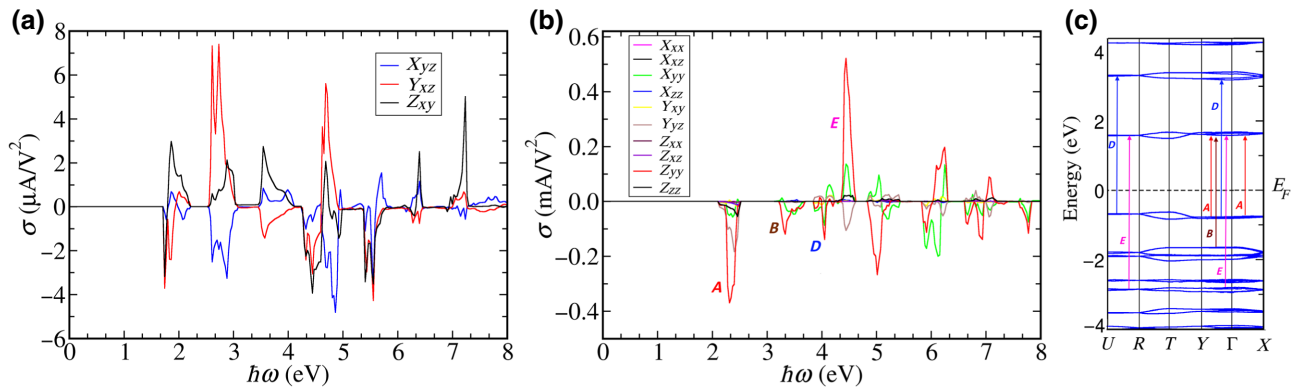

FIG. 4. The calculated photon energy dependence of shift-current tensors of (a) ANA in units of $\mu A/V^2$ and (b) MNA in units of mA/V^2 that is generated by a second-order nonlinear field (σ_{abc}, $\mathbf{a}$, $\mathbf{b}$ and $\mathbf{c} = x, y, z$ axes). The optical transitions occur between bands m and n with energy greater than band gap and so we have resonance absorptions when $\omega = |\omega_{mn\mathbf{k}}|$. The transverse shift current has a large peak along the $Z(X)$ axis due to yy polarized light. The transverse shift current for MNA is larger than the longitudinal one in all energy ranges. (c) The calculated transitions below 5 eV for MNA are marked with vertical arrows in band structure.
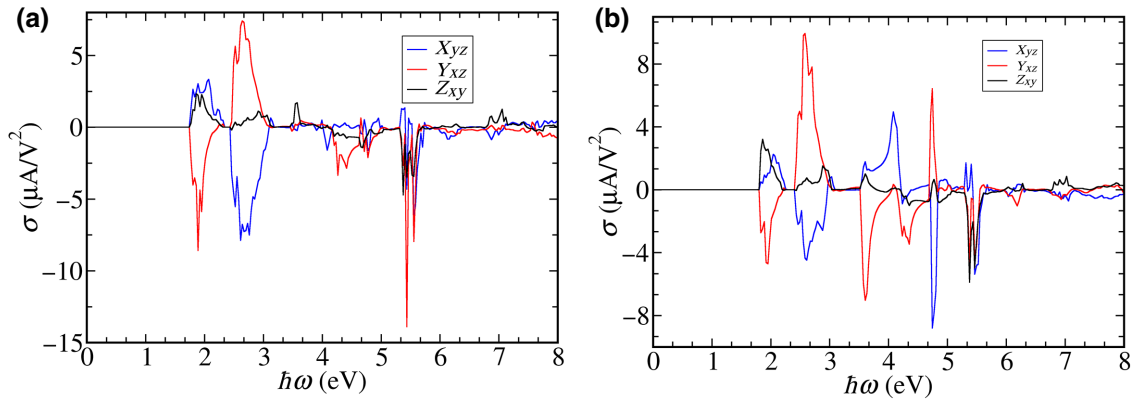
FIG. 5. Comparison of Xyz, Yxz, and Zxy tensor components for (a) -2% compressive strain, and for (b) $+2\%$ tensile strain of ANA in units of $\mu A/V^2$. Imposing uniaxial stretching along the z direction in ANA, the shift current tensors change significantly in comparison with the ones without strain; the peak values depend on the magnitude and type of load applied as well.

similarity between ANA and MNA molecules, the molecular packing along the x axis of ANA increases the band dispersion and gives smaller values of nonlinear response.

Notice that MNA and ANA crystals are almost transparent, except for where they are parallel to molecules [25,47], where the Glass coefficient, defined as σ divided by the absorption, is high. In a similar vein, our calculations' findings (Appendix A) indicate that ANA's absorption coefficients for its yz, xz, and xy components are extremely low (0.01 cm^{-1}), making it nearly transparent in these directions. In contrast to other compounds, the Glass coefficient thus attains considerable values [17,41].

To improve the photovoltaic efficiency of ANA in the visible and infrared, we use a stretching and doping strategy to induce the peak in the shift-current response of ANA in the infrared and visible spectrum. It is worth noting that the same method can be applied to MNA. The application of strain is an extremely challenging tool to modulate

electronic structures, band gaps, and optical responses of materials for photovoltaic applications.

The results of shift-current calculations in Figs. 5 and 6 show that under uniaxial stretching along the z direction in ANA the shift-current tensors change significantly in comparison to the ones without strain, Fig. 4(a). More specifically, the onset of the shift-current-response changes very little depending on the type of load applied, while the peak values depend on the magnitude and type of load applied. In fact, stretching changes the band dispersion and increases the band splitting, leading to an elongation of the energy windows of the shift current as well as their peak value. Figures 5(a) and 5(b) show the shift-current responses under $\pm 2\%$ loading, respectively. Under compressive stress of -2%, the peak values of the shift current above the band gap become larger than those without stress, Fig. 4(a), while under the stress of $+2\%$ they remain practically unchanged, Fig. 5(b). Interestingly, the
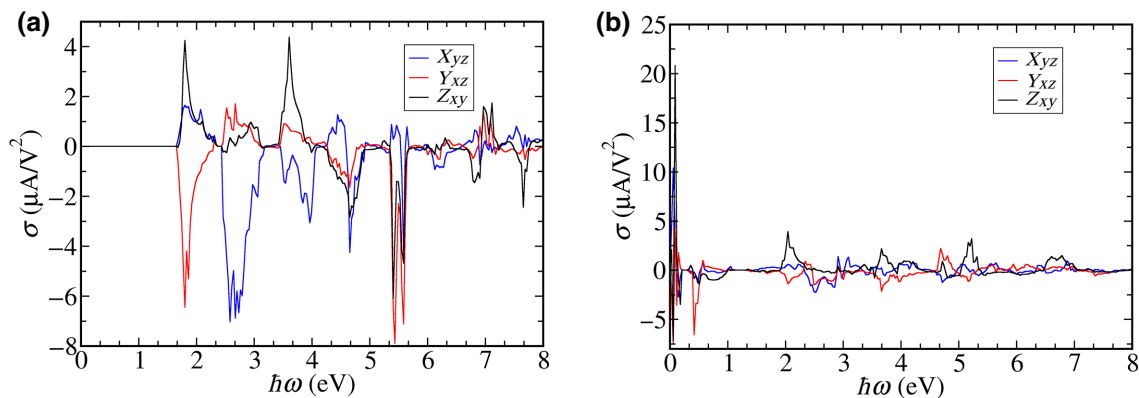

FIG. 6. Comparison of Xyz, Yxz, and Zxy tensor components for (a) -5% compressive strain and undoped of ANA and (b) $+5\%$ tensile strain with hole doped of ANA in units of $\mu A/V^2$. The value of the Fermi energy for $+5\%$ strained ANA is shifted down to 0.03 eV below the valence-band minimum.

strain widens the energy windows of the shift current, in particular, the shift-current responses have nonzero values between 2 and 3 eV under -2% stress. At higher photon energy we can observe the change in direction of the shift currently under stress.

Our calculations show the same behavior for the shift current under $\pm5\%$ strain [see Figs. 6(a) and 6(b)] and the band gap decreases under 5% tensile strain by at most 0.1 eV away, Fig. 6(a). So we try to get the Fermi level right to get the shift current in the infrared. In other words, to account for the tunability of the shift current by regulating the Fermi level of doped ANA, we set the Fermi energy to 0.03 eV below the valence-band minimum in $+5\%$ strained ANA, which is the smallest band gap that the tense structure has. All components above the band edge become twice larger under -5% stress. At higher photon energy the Xyz component becomes dominant while Yxz gradually decreases down to 5 eV. However, in a $+5\%$ strained structure, the shift-current response changes dramatically below 2 eV due to hole doping, Fig. 6(b). We find the large shift current below 1 eV resulting from the transition between the bands from the bands below the Fermi level. In fact, hole doping can be used to induce shift-current responses in the infrared.

It would be worth mentioning that the general results could be applied for strained MNA as obtained for ANA.

IV. CONCLUSION

For the mass photovoltaic effect, molecular crystals with charge-transfer properties are considered attractive candidates. Molecular crystals are notable for their powerful intermolecular and intramolecular charge transfer, which can be further modified using field-effect techniques, as well as stretching and doping molecular crystal structures at high temperatures. We present the molecular crystal structure of 2-methyl-4-nitroaniline and 2-amino-4-nitroaniline as photovoltaic materials with charge transfer originating from electron donor-acceptor groups within molecules using density-functional theory and Wannier interpolation. Even more fascinating, lattice strain along the polarization direction and doping can be used to adjust the shift-current response in these materials. Our calculations show that while stretching has a minimal effect on the band gap, it dramatically changes the shift-current responses across the band edge by modifying the band dispersion and band splitting.

Finally, we would like to highlight possible practical applications of the molecular crystal structure of 2-methyl-4-nitroaniline and 2-amino-4-nitroaniline in comparison to an organic charge transfer complex TTF-CA [15,16]. First of all, as mentioned in this article, this class of photovoltaic materials exhibits both transverse and longitudinal shift-current response over a wide frequency range at high temperatures. Second, these materials exhibit a large shift current, more than 10 times greater than typical reported values for shift current. Third, in the 2-amino-4-nitroaniline molecular crystal, the impressive dependence of the conduction-band dispersion on strain accounts for the photovoltaic tunability in these molecular structures under strain. In addition, doping can be used to improve photovoltaic efficiency in the infrared range.

APPENDIX A: ABSORPTION COEFFICIENT

Here we calculate the absorption coefficient of ANA in Fig. 7 by considering light,

$$E_x = E_0 e^{i\omega\left([k(\omega)/c]z-t\right)} = E_0 e^{-(b(\omega)\omega/c)z} e^{i\omega\left\{[a(\omega)/c]z-t\right\}}, \tag{A1}$$

where c is the speed of light and a and b are the components of the complex refraction index $k(\omega)$,

$$k(\omega) = a(\omega) + ib(\omega), \tag{A2}$$

$$a(\omega) = \sqrt{\frac{1}{2}\left(\epsilon_1 + \sqrt{\epsilon_1^2 + \epsilon_2^2}\right)}, \tag{A3}$$

$$b(\omega) = \sqrt{\frac{1}{2}\left(-\epsilon_1 + \sqrt{\epsilon_1^2 + \epsilon_2^2}\right)}, \tag{A4}$$

where $\epsilon_1(\omega)$ and $\epsilon_2(\omega)$ are the real and imaginary parts of the complex dielectric function, respectively; $\epsilon_r = \epsilon_1 + i\epsilon_2$. Moreover, k and ϵ_r are related to each other through $k^2 = \epsilon_r$. The refractive index is determined by the real part of the dielectric constant, while the absorption is determined by the imaginary part. As $e^{-(2b(\omega)\omega/c)z}$ is the factor
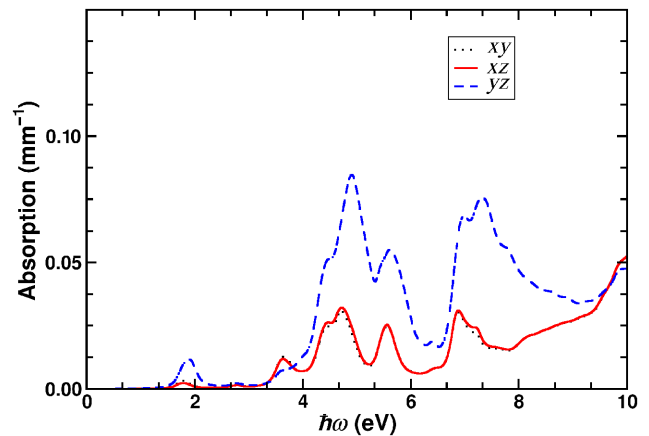

FIG. 7. Absorption coefficients of ANA for $yz, xz,$ and xy components. This shows that ANA is nearly transparent in these directions.

of the light-intensity reduction, we can define absorption coefficient $\alpha(\omega)$

$$\alpha(\omega) = \frac{2b(\omega)\omega}{c} = \frac{\sqrt{2}\omega}{c}\sqrt{-\epsilon_1 + \sqrt{\epsilon_1^2 + \epsilon_2^2}}. \quad (A5)$$

Having calculated the dielectric function in terms of the using the DFT simulations, we can calculate the absorption coefficient based on Eq. (A5). As mentioned in the paper, symmetry in ANA allows shift-current response tensors to have three nonzero independent components Xyz, Yxz, and Zxy. Our calculations shown in Fig. 7 illustrate that the absorption coefficients of ANA are remarkably tiny (≤ 0.01 cm^{-1}) for yz, xz, and xy components and ANA is nearly transparent in these directions.

APPENDIX B: DENSITY OF STATES

Here, we calculate the total density of states (DOS) of MNA and partial density of states for the functional groups of MNA molecule as shown in Fig. 8. These results demonstrate that MNA has a higher DOS around the Fermi level, indicating the lower dispersion of the valence and conduction bands of MNA near the band gap. The high DOS results in nearly flat lower conduction band and the upper valence band in MNA, enhancing nonlinear absorption. ANA molecules exhibit reduced DOS (increased band dispersion) around the Fermi level owing to the higher intermolecular interactions, despite the fact that their structures are identical to those of MNA molecules. Moreover, the Sommerfeld factor implies a peak around the optical transition in the DOS, hence we expect a peak in the current near the optical transition, which indicates the large DOS. The Sommerfeld factor is proportional to the reduced effective mass between the valence and conduction bands, and the inverse of the dielectric constant. Its amplitude depends on material parameters.
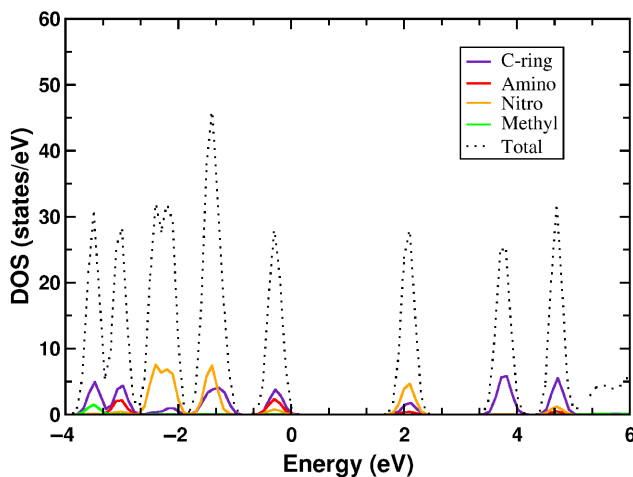

FIG. 8.   Calculated total density of states of MNA and partial density of states for the functional groups of MNA molecule.

In order to have a larger shift current, the system must be polar, and charge carriers must be more mobile due to the configuration of the orbitals of the conduction and valence bands.

[1] E. L. Ivchenko and G. Pikus, *Superlattices and Other Heterostructures: Symmetry and Optical Phenomena* (Springer Science & Business Media, Chicago, 2012), Vol. 110.

[2] B. I. Sturman and V. M. Fridkin, *The Photovoltaic and Photorefractive Effects in Noncentrosymmetric Materials* (Routledge, Chicago, 2021).

[3] V. Fridkin, Bulk photovoltaic effect in noncentrosymmetric crystals, Crystallogr. Rep. **46**, 654 (2001).

[4] A. Chynoweth, Surface space-charge layers in barium titanate, Phys. Rev. **102**, 705 (1956).

[5] V. I. Belinicher and B. I. Sturman, The photogalvanic effect in media lacking a center of symmetry, Sov. Phys. Usp. **23**, 199 (1980).

[6] J. Cheng, N. Vermeulen, and J. Sipe, Dc current induced second order optical nonlinearity in graphene, Opt. Express **22**, 15868 (2014).

[7] W. Shockley and H. J. Queisser, Detailed balance limit of efficiency of *p-n* junction solar cells, J. Appl. Phys. **32**, 510 (1961).

[8] A. M. Cook, B. M. Fregoso, F. De Juan, S. Coh, and J. E. Moore, Design principles for shift current photovoltaics, Nat. Commun. **8**, 14176 (2017).

[9] S. M. Young and A. M. Rappe, First Principles Calculation of the Shift Current Photovoltaic Effect in Ferroelectrics, Phys. Rev. Lett. **109**, 116601 (2012).

[10] D. Xiao, M.-C. Chang, and Q. Niu, Berry phase effects on electronic properties, Rev. Mod. Phys. **82**, 1959 (2010).

[11] R. von Baltz and W. Kraut, Theory of the bulk photovoltaic effect in pure crystals, Phys. Rev. B **23**, 5590 (1981).

[12] T. Morimoto and N. Nagaosa, Topological nature of nonlinear optical effects in solids, Sci. Adv. **2**, e1501524 (2016).

[13] H. Ishizuka and N. Nagaosa, Local photo-excitation of shift current in noncentrosymmetric systems, New J. Phys. **19**, 033015 (2017).

[14] B. M. Fregoso, T. Morimoto, and J. E. Moore, Quantitative relationship between polarization differences and the zone-averaged shift photocurrent, Phys. Rev. B **96**, 075421 (2017).

[15] M. Nakamura, S. Horiuchi, F. Kagawa, N. Ogawa, T. Kurumaji, Y. Tokura, and M. Kawasaki, Shift current photovoltaic effect in a ferroelectric charge-transfer complex, Nat. Commun. **8**, 281 (2017).

[16] B. Kim, J. Kim, D. Shin, M. Choi, J. Lee, and N. Park, Releasing the hidden shift current in the TTF-CA organic molecular solid via symmetry lowering, NPJ Comput. Mater. **6**, 6 (2020).

[17] L. Z. Tan, F. Zheng, S. M. Young, F. Wang, S. Liu, and A. M. Rappe, Shift current bulk photovoltaic effect in polar materials–hybrid and oxide perovskites and beyond, npj Comput. Mater. **2**, 16026 (2016).

[18] T. Rangel, B. M. Fregoso, B. S. Mendoza, T. Morimoto, J. E. Moore, and J. B. Neaton, Large Bulk Photovoltaic

Effect and Spontaneous Polarization of Single-Layer Monochalcogenides, Phys. Rev. Lett. **119**, 067402 (2017).

[19] L. W. Martin and A. M. Rappe, Thin-film ferroelectric materials and their applications, Nat. Rev. Mater. **2**, 1 (2016).

[20] J. Bernstein, *Polymorphism in Molecular Crystals 2e* (International Union of Crystal, Harvard, 2020), Vol. 30.

[21] J. B. Torrance, J. E. Vazquez, J. J. Mayerle, and V. Y. Lee, Discovery of a Neutral-to-Ionic Phase Transition in Organic Materials, Phys. Rev. Lett. **46**, 253 (1981).

[22] S. Horiuchi, T. Hasegawa, and Y. Tokura, Molecular donor–acceptor compounds as prospective organic electronics materials, J. Phys. Soc. Jpn. **75**, 051016 (2006).

[23] M. Dressel and T. Peterseim, Infrared investigations of the neutral-ionic phase transition in ttf-ca and its dynamics, Crystals **7**, 17 (2017).

[24] T. Kolev, B. B. Koleva, M. Spiteller, H. Mayer-Figge, and W. S. Sheldrick, 2-amino-4-nitroaniline, a known compound with unexpected properties, J. Phys. Chem. A **111**, 10084 (2007).

[25] R. Vallée, P. Damman, M. Dosiere, E. Toussaere, and J. Zyss, Nonlinear optical properties and crystalline orientation of 2-methyl-4-nitroaniline layers grown on nanostructured poly (tetrafluoroethylene) substrates, J. Am. Chem. Soc. **122**, 6701 (2000).

[26] G. Ferguson, C. Glidewell, J. N. Low, J. M. Skakle, and J. L. Wardell, Hydrogen bonding in c-methylated nitroanilinesthe three-dimensional framework structure of 2-methyl-4-nitroaniline, Acta Crystallogr., Sect. E: Cryst. Struct. Commun. **57**, 315 (2001).

[27] R. Morita, T. Kondo, Y. Kaneda, A. Sugihashi, N. Ogasawara, S. Umegaki, and R. Ito, Dispersion of second-order nonlinear optical coefficient d11 of 2-methyl-4-nitroaniline (MNA), Jpn. J. Appl. Phys. **27**, L1131 (1988).

[28] C. Grossman and A. Garito, Brewster angle method for refractive index measurements of biaxial organic systems, Mol. Cryst. Liq. Cryst. **168**, 255 (1989).

[29] P. Hohenberg and W. Kohn, Inhomogeneous electron gas, Phys. Rev. **136**, B864 (1964).

[30] W. Kohn and L. J. Sham, Self-consistent equations including exchange and correlation effects, Phys. Rev. **140**, A1133 (1965).

[31] P. Blaha, K. Schwarz, G. K. Madsen, D. Kvasnicka, and J. Luitz, in *WIEN2k, An Augmented Plane Wave Plus Local Orbitals Program for Calculating Crystal Properties* (TU Vienna, Vienna, 2001), Vol. 60.

[32] P. Giannozzi, *et al.*, Quantum espresso: A modular and open-source software project for quantum simulations of materials, J. Phys.: Condens. Matter **21**, 395502 (2009).

[33] J. P. Perdew, K. Burke, and M. Ernzerhof, Generalized Gradient Approximation Made Simple, Phys. Rev. Lett. **77**, 3865 (1996).

[34] J. E. Sipe and A. I. Shkrebtii, Second-order optical response in semiconductors, Phys. Rev. B **61**, 5337 (2000).

[35] H. Presting and R. Von Baltz, Bulk photovoltaic effect in a ferroelectric crystal a model calculation, Phys. Status Solidi (b) **112**, 559 (1982).

[36] R. D. King-Smith and D. Vanderbilt, Theory of polarization of crystalline solids, Phys. Rev. B **47**, 1651 (1993).

[37] C. Aversa and J. E. Sipe, Nonlinear optical susceptibilities of semiconductors Results with a length-gauge analysis, Phys. Rev. B **52**, 14636 (1995).

[38] J. Ibañez-Azpiroz, S. S. Tsirkin, and I. Souza, Ab initio calculation of the shift photocurrent by Wannier interpolation, Phys. Rev. B **97**, 245143 (2018).

[39] R. E. Newnham, in *Properties of Materials* (Oxford University Press, Chicago, 2005).

[40] R. R. Boyd, *Nonlinear Optics* (Elsevier, New York, 2008).

[41] R. Fei, L. Z. Tan, and A. M. Rappe, Shift-current bulk photovoltaic effect influenced by quasiparticle and exciton, Phys. Rev. B **101**, 045104 (2020).

[42] J. Ibañez Azpiroz, S. S. Tsirkin, and I. Souza, Ab initio calculation of the shift photocurrent by Wannier interpolation, Phys. Rev. B **97**, 245143 (2018).

[43] B. M. Fregoso, Bulk photovoltaic effects in the presence of a static electric field, Phys. Rev. B **100**, 064301 (2019).

[44] R. P. Tiwari, B. Birajdar, and R. K. Ghosh, First-principles calculation of shift current bulk photovoltaic effect in two-dimensional α-In$_2$Se$_3$, Phys. Rev. B **101**, 235448 (2020).

[45] J. Ibañez-Azpiroz, I. Souza, and F. de Juan, Directional shift current in mirror-symmetric BC$_2$N, Phys. Rev. Res. **2**, 013263 (2020).

[46] Y. Zhang, F. de Juan, A. G. Grushin, C. Felser, and Y. Sun, Strong bulk photovoltaic effect in chiral crystals in the visible spectrum, Phys. Rev. B **100**, 245206 (2019).

[47] B. Levine, C. Bethea, C. Thurmond, R. Lynch, and J. Bernstein, An organic crystal with an exceptionally large optical second-harmonic coefficient 2-methyl-4-nitroaniline, J. Appl. Phys. **50**, 2523 (1979).